Materials Advances

ROYAL SOCIETY OF CHEMISTRY

PAPER

View Article Online
View Journal | View Issue

Cite this: *Mater. Adv.*, 2025, 6, 3969

A photodegradation study of the deposition fabricated CdS–$BiVO_4$ binary catalyst: a brief comparison with other fabrication procedures†

Pooneh Hemmatpour, Alireza Nezamzadeh-Ejhieh * and Ali Ershadi

Received 18th March 2025,
Accepted 25th April 2025

DOI: 10.1039/d5ma00240k

rsc.li/materials-advances

In the present study, Eriochrome black T (EBT) degradation in an aqueous environment was carried out by CdS–$BiVO_4$ integrated catalysts prepared using several integrated methods. The catalyst prepared *via* the deposition method showed the highest activity. The catalysts were identified using XRD, FTIR, SEM, UV-Vis DRS, and cyclic voltammetry (CV). The crystallite size of the binary catalyst was obtained at about 25.3 nm and 45 nm by the Scherrer and Williamson–Hall methods. Since the response surface methodology (RSM) is one of the efficient modeling methods, it was used to investigate the simultaneous effects of the effective parameters (catalyst amount, pollutant concentration, pH, and irradiation time) on the photocatalytic degradation. R^2 showed good agreement between the experimental results and the data predicted by the software. Also, the predicted square model was very satisfactory with high correlation coefficients R^2 (0.9839) and adj R^2 (0.9688). The optimal-run conditions were C_{EBT}: 15 ppm, catalyst dose: 0.9 g L^{-1}, pH: 7.3, and illumination time: 20 min. The effect of some inhibitory agents was evaluated, and it was found that the role of superoxide radicals and the holes in the degradation of EBT is more critical than that of hydroxyl radicals and photoinduced electrons, based on the direct Z-scheme mechanism proposed for charge carriers' transfer. The process obeyed a pseudo-first-order kinetic with the apparent rate constant of 0.0614 min^{-1}.

1. Introduction

Of the more than 7×10^7 tons of annual worldwide production of synthetic dyes, textile industries contribute more than 1×10^4 tons of these dyes in wastewater. Dye-polluted wastewater resulting from the discharging of textile industries' effluents, including various persistent pollutants, has created a critical environmental crisis because of the critical effects of this type of wastewater on human health and life bodies, in general.[1–3] These textiles increase the biochemical and chemical oxygen demand (BOD and COD) and thus destroy water bodies' esthetic quality, disrupting photosynthesis, diminishing plant growth, and entering the food chain and creating recalcitrance and bioaccumulation acting as potentially toxic, mutagenic, and carcinogenic resources.[1,4,5]

Azo dyes, which contain one or more azo groups structurally, are the largest class.[6] Above 60% of textile dyes consist of azo dyes.[7,8] Because of inefficient textile dyeing processes (not bound to fibers and fabrics), about 15–50% of these azo dyes are commonly released into corresponding wastewater, finally discharging into water bodies, causing severe ecotoxicological threats and toxic effects on living organisms.[9] Farming with untreated wastewater of such industrial effluents harms soil quality and crop germination rates.[1,10] The reduced light penetration due to the discharged azo dyes into water impairs aquatic plants' algae activity and growth. Metabolization of the ingested dyes by fish and living organisms produces toxic intermediates in their bodies, causing adverse effects on the fish and their predators' health.[11] *Via* oral ingestion or direct skin exposure to industrial effluents containing azo dyes, humans and other mammals are affected by the hazardous effects of azo dyes.[12] The conversion of azo dyes into toxic amino acids by human gut intestinal microflora, induces adverse effects on some human body tissues.[13,14] Moreover, carcinogenic amines can be produced *via* azo dyes' degradation by cultured bacteria from human skin.[1,15]

One such azo dye is eriochrome black T (EBT) ($C_{20}H_{12}N_3NaO_7S$), which is a dye pre-treated with chromium salts that has wide application in silk, wool, and nylon fiber coloring (contributing above 50% of the global dye production). In contrast, its pure form has wide application in complexometric titration indicators for Ca(II), Mg(II), Zn(II), and other ions.[16,17]

Department of Chemistry, Shah. C., Islamic Azad University, P.O. Box 311-86145, Shahreza, Isfahan, Islamic Republic of Iran. E-mail: chemisthemmat@yahoo.com, ali_ershadi@iau.ac.ir, arnezamzadeh@iau.ac.ir, arnezamzadeh@iaush.ac.ir, arnezam1346@gmail.com, Alireza_nezamzadeh@yahoo.com

† Electronic supplementary information (ESI) available. See DOI: https://doi.org/10.1039/d5ma00240k

Its release into natural waters critically affects the photosynthetic activities in aquatic systems. It produces carcinogenic naphthoquinone and degradation products, finally producing lethal effects when present in drinking and surface water.[18] Generally, it is challenging to withdraw EBT from water even in low concentrations because it has high resistance against heat and light, as well as against water, chemical agents, and bacteria. Thus, removing even low concentrations of EBT is a critical challenge.[19,20]

Due to the importance of investigating pollutant detection, human health, *etc.*, several degradable and novel sensors have been introduced.[21–23] The synthetic dyes' durability and solubility in water makes it difficult for conventional treatment strategies to remove them,[24,25] and due to creating secondary pollution and the incomplete removal efficiency of these traditional strategies, there is a critical need for the use of advanced cost-effective and environmentally friendly approaches to adequately decrease dye-pollution in such wastewater before it is discharged into the environment.[1,26] This effective strategy is heterogeneous photocatalysis *via* the illumination of a typical semiconducting material by UV or visible photons with sufficient energy equal to or greater than the semiconductor energy bandgap (E_g).[27,28] Under the illumination process, the photoexcitation of the electrons to the conduction band (CB) leaves the holes in the valence band (VB), which can respectively react with the dissolved oxygen and water molecules (or hydroxyl anions) to generate superoxide and hydroxyl radicals as powerful reactive species.[29,30] Thus, a typical photodegradation process's overall efficiency is affected by these four reactive species, including the photoinduced electron–hole (e/h) pairs and powerful superoxide and hydroxyl radicals.[31,32] Unfortunately, the overall process efficiency drastically diminishes with e/h pair recombination.[33,34] Thus, to have an efficient photocatalytic process, this negative process should be overcome by a suitable strategy like doping of metals or nonmetals,[35] supporting of semiconductors onto a support,[29] heterojunction construction[28] and coupling of two or more semiconductors,[36–38] vacancy and defects induction,[39,40] plasmonic systems, *etc.*[35]

Metal oxides have been broadly used in various fields.[41] Bismuth vanadate ($BiVO_4$), a potential visible-light active semiconducting material photocatalyst, has shown high stability and excellent photocatalytic activity primarily when a piezophotocatalytic $BiVO_4$ is used.[42,43] From a thermodynamic point of view, the stability of three $BiVO_4$ crystallites is in the sequence of monoclinic scheelite (ms-$BiVO_4$) > tetragonal scheelite (ts-$BiVO_4$) > tetragonal zircon (tz-$BiVO_4$),[44] with an excellent visible-light photocatalytic activity for ms-$BiVO_4$ that can be obtained during high-temperature synthesis (solid-state and melting reactions) (low-temperature synthesis commonly forms tz-$BiVO_4$).[45] Various factors, including the particle size and grain morphology, the effective surface area and the crystallographic plane ratio, affect the ms-$BiVO_4$ photocatalytic activity.[46] Low-temperature synthesis of ms-$BiVO_4$ improves its specific surface area while reducing its crystallinity and photocatalytic activity. One way to have a good crystallin photocatalyst with a high surface area at a lower temperature is to synthesize it with an ionic liquid.[47] So far, various microwave-assisted $BiVO_4$ synthesis strategies,[48] including strawberry-like structured $BiVO_4$,[49] different $BiVO_4$ morphologies at different pH,[50] Tb^{3+}–$BiVO_4$,[51] and sandwich-like $BiVO_4$[49,52] have been synthesized and little attention has been paid to the effects of the change in reactants and morphologies control.[53] A ternary SnO_2–$BiVO_4$–CuO system also showed boosted photocatalytic activity compared with the individual catalysts.[54]

CdS, as an n-type semiconductor, is known to be a compelling photocatalyst because of its excellent features, such as excellent optical visible-light absorption, its narrow band gap of 2.4 eV, and its simple synthesis procedure. Unfortunately, its limited photocatalytic application has been reported due to fast e/h pair recombination and its easy photo-corrosion.[55,56] Due to the limitations of $BiVO_4$ and CdS mentioned above, some strategies such as constructing a Z-scheme $BiVO_4$/CdS photocatalytic system,[51,57,58] coupled $BiVO_4$/rGO/CdS system,[59] *etc.* have been reported.

Based on the discussion illustrated above, we were prompted to study the effects of some preparation methods to construct a binary $BiVO_4$/CdS photocatalyst in the EBT photodegradation process. In the first fabrication procedure, this binary catalyst was prepared mechanically by a grinding method and was well characterized and used in EBT photodegradation. The process kinetics and mechanism were well studied in our previous works.[60,61] Continuing this work, we used a deposition method and other techniques to fabricate binary $BiVO_4$/CdS photocatalysts. Due to the best activity of the binary catalyst prepared *via* the deposition methods (D-BS), this catalyst was used for further investigation. Here, the results of its brief characterization will be discussed. Then, the photodegradation conditions optimized by the RSM approach and the corresponding photodegradation mechanism will be discussed. Some binary catalysts were also prepared with sonication on the binary catalysts prepared by mechanical and simple physical mixing approaches in the presence of aqueous and organic solvents. The degradation efficiencies of the prepared photocatalysts in EBT degradation will also be briefly compared.

2. Experimental section

2.1. Synthesis of CdS and $BiVO_4$ NPs and fabrication of the binary catalyst

Detailed procedures for the synthesis of CdS nanoparticles (CdS NPs) using cadmium nitrate and ammonium sulfide have been reported in our previous studies[60,61] and in the literature.[62] Furthermore, the hydrothermal procedure used to synthesize $BiVO_4$ NPs using ammonium vanadate and bismuth nitrate has been described in detail in our previous studies[60,61] and in the literature.[63] All chemicals used throughout the work were of analytical grade purity and purchased from Flucka/Alrdrich Co.

To fabricate a binary $BiVO_4$/CdS photocatalyst *via* a deposition method, 2.618 g of cadmium nitrate tetrahydrate was dissolved in water and diluted in a 100 mL flask. After adding this into a 250 mL beaker on a magnetic stirrer, 2.748 g of

pre-synthesized bismuth vanadate was added and stirred for one hour. Many Cd(II) cations were adsorbed onto the $BiVO_4$ surface during the stirring process. In the next step, 0.68 mL ammonium sulfide was diluted to 100 mL. It was added very slowly during several steps to the previous solution under vigorous stirring, and a stirring process was continued for another hour to complete the precipitation of CdS NPs onto the $BiVO_4$ surface. The final intended sediment was separated *via* centrifugation (at 13 000 rpm for 10 min), washed 3–4 times with distilled water, and dried at room temperature for 24 h. Our research group suggested this procedure, and some conditions were adopted from the literature.[64] This binary catalyst was named deposited catalysts and abbreviated as D-BS.

In fabricating by the mechanical grinding mixed system, 30 mg of the as-synthesized CdS NPs and 770 mg of the as-synthesized $BiVO_4$ NPs were added into an agate mortar and thoroughly hand-mixed for 10 min, and the catalyst was named Gr-BS. Similar samples were also prepared and ultrasonicated in water (1 mL water, at 40 °C and 37 kHz for 10 min), named WUS-Gr-BS, and in hexane (1 mL hexane under similar conditions), named HUS-Gr-BS.

Another strategy used here to fabricate the binary BS catalyst was simple mechanical mixing with no grinding process. For this goal, 30 mg of the as-synthesized CdS NPs and 770 mg of $BiVO_4$ NPs were added to a dish and thoroughly hand-mixed for 10 min. This sample was named MMix-BS. A similar weight of the individual catalysts was also mixed and then ultrasonicated in water (WUS-MMix-BS) and hexane (HUS-MMix-BS) under the same conditions applied for the ultrasonicated Gr-BS in the above paragraph.

2.2. Samples' characterization

The characterizing instruments used here are summarized below. An XRD diffractometer (X'PertPro, Netherland, with Cu-Kα radiation at 1.5406 Å), an absorption FT-IR spectrophotometer (PerkinElmer Spectrum 65), a UV-Visible diffuse reflectance spectrophotometer (DRS, JASCO V 670 instrument, Japan), and a scanning electron microscope (SEM, Seron technology, model: AIS2100). Modified carbon paste electrodes (CPE) by the individual or binary catalysts (10 w% for the modifier) were fabricated as described in the literature.[65] Cyclic voltammograms (CVs) were obtained over a potentiostat/galvanostat (Autolab, PGSTAT-101, EcoChemie, Netherlands) equipped with the modified CPE (working electrode), in the presence of a platinum rod electrode (auxiliary electrode) and Ag/AgCl electrode (3 M KCl solution, reference electrode). The similar working electrode had a geometric surface area of 0.0314 cm^2 (for an id of 2 mm) and an effective surface area of about 0.265 cm^2.[65]

The pHpzc of the catalysts was also determined by recording the change in the pH of suspensions (15 mg in 5 mL of each catalyst in 0.05 M NaCl solution as an ionic strength adjustment) after 24 h shaking when the initial pH values were adjusted in the range of 2–12 by dilute HCl or NaOH solution.

2.3. Investigating the degradation of EBT pollutant

A series of 10 mL of 10 ppm Eriochrome black T solutions containing 3 mg of the catalyst (equivalent to 0.3 g L^{-1}) at pH 6 were prepared in 25 mL glass beakers and used for carrying out the surface adsorption process (in the absence of light), or photodegradation process in the presence of 3 tungsten lamps (30 W) positioned 10 cm above the reaction cell under a 30 min illumination process, after the centrifugation process (at 13 000 rpm for 5 min). Then, the absorption of the supernatant was recorded (A) and against that of the control solution (an EBT solution with the same concentration but with no catalyst and irradiation) (A_0) by an ultraviolet-visible spectrophotometer at the EBT maximum wavelength (530 nm). The decrease in absorption intensity of the photodegraded solution shows the degree of pollutant degradation calculated by the following equation. It is worth mentioning that based on the correspondence of A and C (the pollutant concentration) according to the Beer–Lambert law, the absorbance values have been used here for easy calculation of the degradation percentage of EBT.[60,61]

$$\text{Degradation\%} = [(C_0 - C)/C_0] \times 100 = [(A_0 - A)/A_0] \times 100 \quad (1)$$

3. Results and discussion

3.1. Characterization results

3.1.1. Powder XRD identification. Fig. 1(A) compares the diffraction patterns of individual and coupled samples. Diffraction index lines for the as-synthesized CdS NPs at 2θ angles equal to 26.81° (111), 42.20° (220), 82.51° (311), and 71.51° (331), corresponding to the CdS cubic phase (JCPDS: 0440-89), were observed. By measuring the peak width of the sample pattern and using the Scherer equation, the average crystal size in the tested sample was 5.8 nm.[42] It is worth mentioning that some characterization data, especially for the individual CdS NPs and $BiVO_4$ NPs, including XRD pattern FTIR spectra, SEM-EDX results and X-ray maps, and CVs may be presented and discussed in our previous parts of this work.[60,61]

Diffraction index lines for the prepared bismuth vanadate sample were observed at 2θ angles equal to 18.9°, 28.9°, 30.6°, 34.5°, 35.2°, 39.8°, 42.4°, 50.1°, 53.2°, and 58.3° corresponding to Miller indices of (011), (121), (040), (200), (002), (211), (051), (202), (161) and (201), which agree with the monoclinic scheelite structure of $BiVO_4$ based on JCPDS: 14-0688.[66,67] The Scherer equation estimated the crystal size of 34.9 nm for $BiVO_4$ NPs. XRD patterns of the individual CdS and $BiVO_4$ NPs have been well discussed in our previous studies.[60,61]

In the pattern of the coupled binary CdS/$BiVO_4$ catalyst, some characteristic lines for the CdS nanocrystals were observed at 2θ angles of 44.42°, 52.72°, and 69.65° degrees.[68] In this pattern, the presence of $BiVO_4$ nanocrystals was confirmed by the appearance of typical diffraction peaks at 2θ angles equal to 19.19, 29.25, 30.70, 32.61, 22.35, 40.40, 42.67, 47.04, 50.11, 53.45 and 59.15 degrees.[69] The comparison between the X-ray diffraction patterns of the integrated CdS/$BiVO_4$ photocatalyst and CdS and $BiVO_4$ individual nanocrystals shows a good overlap for the characteristic lines of both samples.[70] The broadening of the peaks can indicate CdS/$BiVO_4$

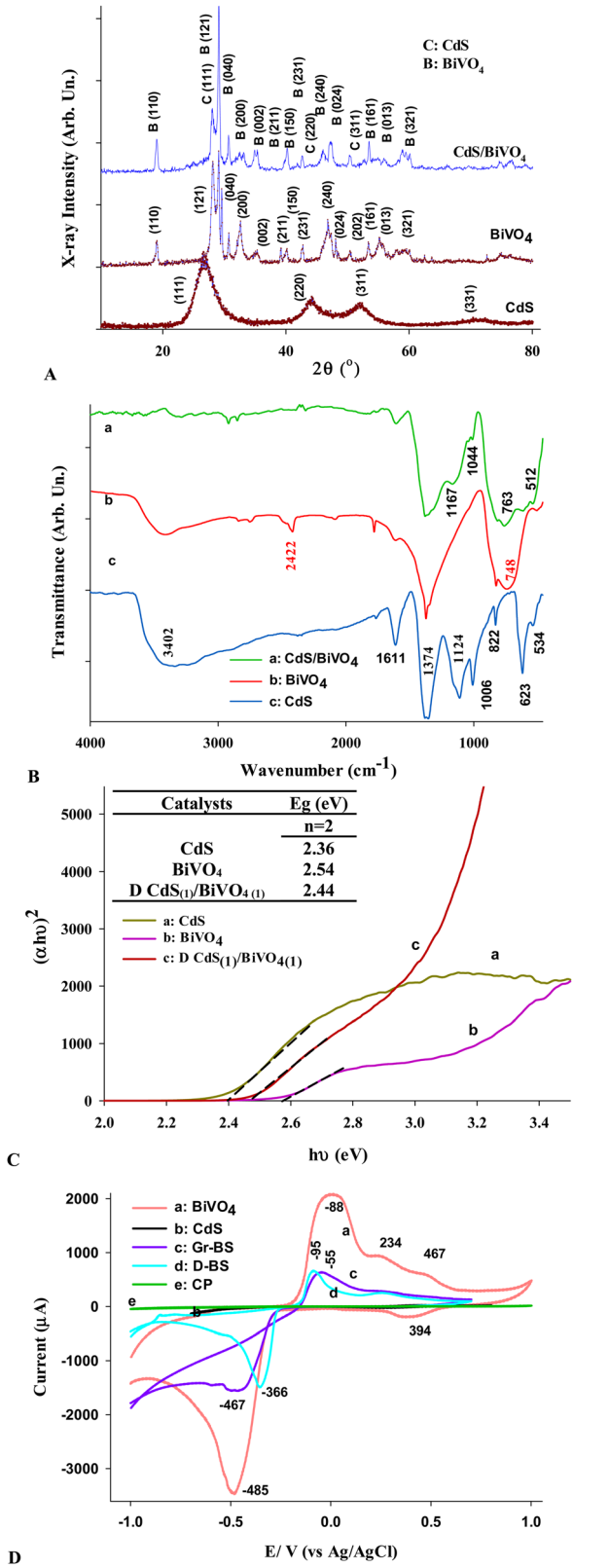

Fig. 1 XRD patterns (A), FTIR spectra (B),[60,61] typical Tauc plots (C), and CVs (D) for the individual and coupled samples.

crystal size reduction. The comparison of the patterns shows that in all the patterns of the modified samples, cadmium sulfide and bismuth vanadate indicator peaks are observed. Still, due to the combination of cadmium sulfide and bismuth vanadate photocatalysts, the intensity of the indicator peaks has been relatively reduced. To some extent, the position of the photocatalyst peaks of cadmium sulfide is partially displaced.[48] According to Scherer's results, the crystal size of the $CdS/BiVO_4$ integrated catalyst is 25.3 nm.

The X-ray diffraction device has many applications, the most important of which is the detection of crystalline phases. The size of the crystallites was calculated using the following Debye–Scherer equation.[71,72]

$$D = \frac{K\lambda}{\beta \cos\theta}$$

where d is the size of the crystals, λ is the wavelength, Cu-Kα is equal to 0.154 nm corresponding to the X-ray diffraction device, K shape factor is equal to 0.9, β is the width of the peak at half its height, and θ is the location of the peak on the horizontal axis of the diffraction pattern.[73]

One of the drawbacks of Scherer's method is that it considers the broadening of the peaks only due to the size of the crystals and is unsuitable for materials with strain. The studies conducted by Williamson–Hall (W–H) showed that the peak broadening at half maximum intensity (FWHM) is a function of the grain size and the intra-lattice strains. The Williamson–Hall equation is given as follows.

$$\beta_T \cdot \cos\theta = \varepsilon \sin\theta + (K\lambda)/D$$

In this equation, β is the peak width at half height or FWHM in radians, θ is the angle at which the re-irradiated rays have the largest amplitude compared to the original radiation beam, ε is the strain rate of the sample, K is the shape factor, here 0.9 is considered, λ is the Kα wavelength of the corresponding anode of the device, D is the crystal size whose unit is equal to the λ unit (nanometers or angstroms). It is clear from the type of equation that if the data related to $\beta_T \cdot \cos\theta$ in terms of $\sin\theta$, a straight line will be obtained, which gives strain from its slope and the size (d) from the intercept. The used data and figures are presented in SDT1-2 and SDF1 (see the ESI†). The W–H model gave the coupled catalyst a crystallite size of about 45 nm.

3.1.2. FT-IR characterization of the samples. Fig. 1(b) shows the FT-IR absorption spectra of CdS, $BiVO_4$, and the coupled $CdS/BiVO_4$ nanoparticles. All spectra contain absorption bands related to the absorbed water (the stretching band at about 3500 cm^{-1} and bending vibration in the region of about 1640 cm^{-1}) and bands related to organic substances used during the synthesis of nanoparticles.[74] A wide band between 3140–3470 cm^{-1} can be seen, which is related to the O–H stretching vibrations.[75] Also, the absorption bands at 541 cm^{-1} and 663 cm^{-1} correspond to the vibration of the Cd–S and S–S bands in the cadmium sulfide crystal, respectively.[76]

Bismuth vanadate shows intense and broad bands at 843 cm^{-1} and 642 cm^{-1}, which are attributed to the symmetric and asymmetric V–O stretching vibrations. Also, the band at 1058 cm^{-1} is attributed to the V=O group. The stretching

vibrations of the bonded oxygen shared by the two V–O–V vanadium atoms give rise to a band at 642 cm^{-1} corresponding to the symmetric V–O–V stretching state.[77] The band at 408 cm^{-1} is due to Bi–O bending vibrations. In general, all absorption bands of CdS and $BiVO_4$ photocatalysts are observed in the absorption spectrum of the CdS/$BiVO_4$ binary coupled photocatalyst prepared by the deposition method.[69] FTIR spectra of the individual CdS and $BiVO_4$ NPs have been well discussed in our previous studies.[60,61]

3.1.3. Characterization by diffuse reflectance spectroscopy (DRS). Energy gaps (E_g) are mainly measured directly by visible-reflectance-ultraviolet transmission spectroscopy on a thin film or compressed powder surfaces. Energy gaps in semiconductors are classified into two groups: direct and indirect. In a semiconductor with a direct energy gap, the structure of energy levels has a maximum level in the valence band (VB) and a minimum level in the conduction band (CB), which have the same values of (K).[78] When the electron is transferred from the conduction band to the valence band with the emission of energy $E = h\nu$, the size of the movement does not change because (K) has not changed. In a semiconductor with an indirect energy gap, the electron has not changed from the conduction band to the valence band. In a semiconductor with an indirect energy gap, the electron moves from the conduction band to the valence band. It changes the size of the movement because the (K) values change, and the energy is released as heat instead of photon emission, resulting in the minimum of the conduction band *versus* the maximum of the band. The capacity is not placed. The Kubelka–Munk radiative transfer model allows reflectance calculation by an edge that absorbs and emits light. According to the assumptions of this model, the reflection data can be processed with the following equation.[25]

$$K = (1 - R)^2/2R$$

The energy gap of synthetic semiconductors is determined by the Kubelka–Munk method and by using Tauc diagrams and the visible absorption spectrum. For this purpose, the following Beer–Lambert law and Tauc's formula are used to obtain the energy gap.[79]

$$A = -\log(I/I_0)$$

$$(\alpha h\nu) = K(h\nu - E_g)^2 \text{ or } (\alpha h\nu)^{1/2} = K(h\nu - E_g)^n$$

In the beer–Lambert law, 'I' is the transmitted light intensity concerning the primary light intensity I_0, and A is the absorbance of the sample. In the Tauc formula, K is a constant coefficient, and E_g is the energy gap. In the Tauc formula, n indicates the nature of the transfer and has different values of 1/2, 2, 3/2, and 3 times direct allowed, indirect allowed, direct not allowed, and indirect not allowed, respectively. All Tauc formulas are also summarized in Table 1. Various Tauc formula formats have been well illustrated in the literature.[80]

The corresponding absorption spectra of the penetration reflectance spectra of CdS, $BiVO_4$, and CdS/$BiVO_4$ nanoparticles are shown in SDF2A (ESI†). By converting the reflectance data of UV-Vis spectra using the Kubelka–Munk equation and drawing Tauc–Goff diagrams, the energy of direct and indirect transfers for photocatalysts was also calculated, and the corresponding curves are shown in Fig. 1(C) and SDF2-B–E (ESI†). Typical Tauc plots and the reflectance spectra of the individual CdS and $BiVO_4$ NPs have been well discussed in our previous studies.[60,61]

Table 1 Optical data and the sample's VB/CB potential positions[60,61]

Band gap energies

	Tauc plots (eV)				Absorption edge	
Catalysts	1/2	2	3/2	3	λ (nm)	E_g (eV)
CdS	2.10	2.36	2.29	2.37	566	2.19
BiVO4	2.39	2.54	2.51	2.57	621	1.99
CdS–$BiVO_4$	2.31	2.56	2.55	2.61	540	2.29

Elemental E_a and E_i values[60,61]

Element	E_a (eV)	E_i (eV)	$1/2(E_a + E_i)$ (eV)
Cd	0.724	8.985	4.854
S	2.077	10.358	6.217
Bi	0.942	7.238	4.090
V	0.527	6.739	3.633
O	1.461	13.618	7.539

Mulliken's electronegativities and potential positions

Catalyst	χ (eV)	E_g (eV)	E_{VB} (eV)	E_{CB} (eV)
CdS	5.49	2.36	+2.07	−0.28
$BiVO_4$	5.98	2.54	+2.77	+0.18

Various formulas for writing the Tauc model

	n-value for:				
Formula	IF	IA	DF	DA	Ref.
$F(R)\ h\nu = A\ (h\nu - E_g)^n$	3	2	3/2	1/2	81
$(F(R)\ h\nu)^n = A\ (h\nu - E_g)$	1/3	1/2	2/3	2	82
$(\alpha h\nu)^{1/n} = A\ (h\nu - E_g)$	3	2	3/2	1/3	83–85
$(\alpha h\nu) = A\ (h\nu - E_g)^{1/n}$	1/3	1/2	2/3	2	86,87
$(\alpha h\nu) = A\ (h\nu - E_g)^{n/2}$	6	4	3	1	88
$(\alpha h\nu)^{2/n} = A\ (h\nu - E_g)$	6	4	3	1	88

By using the obtained E_g for single photocatalysts CdS and $BiVO_4$ for $n = 2$ and the following formulas, the potential of the VB and CB positions was also calculated.

$$E_{VB} = X - E_e + 0.5\ E_g$$

$$E_{CB} = E_g - E_{VB}$$

In this equation, E_e is the free electron energy compared to NHE (equal to 4.5 eV), χ is the absolute electronegativity, and χ is the geometric mean electronegativity of the constituent atoms, which is obtained through the following equation. Also, a and b are the numbers of A and B atoms in the semiconductor.

$$X = [\chi_{(A)}{}^a\ \chi_{(B)}{}^b]^{1/(a+b)}$$

All data and information used/obtained in these calculations are summarized in Table 1. The corresponding values for

the individual CdS and $BiVO_4$ NPs have been well discussed in our previous studies.[60,61]

3.1.4. Characterization by cyclic voltammetry (CV). The electrochemical behavior of the modified carbon paste electrode (CPE) with CdS, BiVO4 single catalysts and CdS/$BiVO_4$ combined catalysts prepared by grinding (Gr-BS) and deposition (D-BS) methods were investigated, and the corresponding cyclic voltammograms are compared in Fig. 1(D). The applied potential was −0.1 to 1 V, the scanning speed was 50 mV s^{-1}, and the 0.1 M sodium hydroxide solution electrolyte with pH 13 was used. As shown by the CVs, for the voltammogram (e), which is related to the bare CPE, no oxidation or reduction peaks were observed due to the absence of active electrons. Similarly, no voltammetric current was also observed for the modified electrode by CdS NPs. When the modified carbon paste electrode with $BiVO_4$ NPs was used, the apparent intense CV peak currents were observed, which can be related to redox reactions of Bi(III)/Bi(IV) and vanadium oxidation states. The peak currents showed a critical decrease concerning the $BiVO_4$-CPE by modifying CPE with both coupled Gr-BS and D-BS systems. This decrease conforms to the internal charge transfer between CdS and $BiVO_4$ in the coupled system, resulting in a smaller charge transfer in the external circuit. It was concluded that the combined catalyst had better charge transfer than other catalysts.

3.1.5. SEM-EDX and map analysis. As shown in Fig. 2(A)–(C), the CdS/$BiVO_4$ combined photocatalyst is completely nanospherical and looks homogeneous and uniform in terms of morphology. In the planting method, the particles have become slightly larger, but the uniformity of the particle size has increased. Due to the small size of the particles, more accumulation and consolidation can be seen in all nanoparticles. The estimated average particle size was obtained by applying ImageJ software on the images to be about 56 to 97 nm, which confirms the presence of photocatalyst nanoparticles and agrees with the results obtained using Scherer's equation. It is worth mentioning that XRD gives us a crystallite size that is relatively smaller than the particle size because particles consist of many crystallites.

Energy dispersive spectroscopy (EDX) is used to analyze the elements in the sample and install it on electron microscopes to perform both qualitative and quantitative analysis. Fig. 2(D) (and Table SD3, ESI†) shows the combined CdS/$BiVO_4$ photocatalyst prepared by deposition method consisting of sulfide, vanadium, bismuth, oxygen, and cadmium elements. In other words, no impurities are visible in the investigated range. In the studied sample, the molar ratio for combining two catalysts was 1 : 1, equivalent to the equal weight ratio of two catalysts. However, the results showed a higher weight percentage of vanadium bismuth in the combined catalyst. Considering that the relevant analysis is carried out superficially and examines only one point of the sample, if the recorded spectrum corresponds to a point where the scattering of semiconductor particles among each other is not done well, in percent by weight contrary to values becomes real.

The X-ray maps prepared from the consolidated sample using the CdS/$BiVO_4$ deposition method in Fig. 2(E) and SDF3 (ESI†) show the almost uniform and homogenous distribution of oxygen, sulfide, cadmium, vanadium, and bismuth elements in the consolidated sample, which makes it perform more reproducibly in the catalytic process. Some data for the individual CdS and $BiVO_4$ NPs have been well discussed in our previous studies.[60,61]

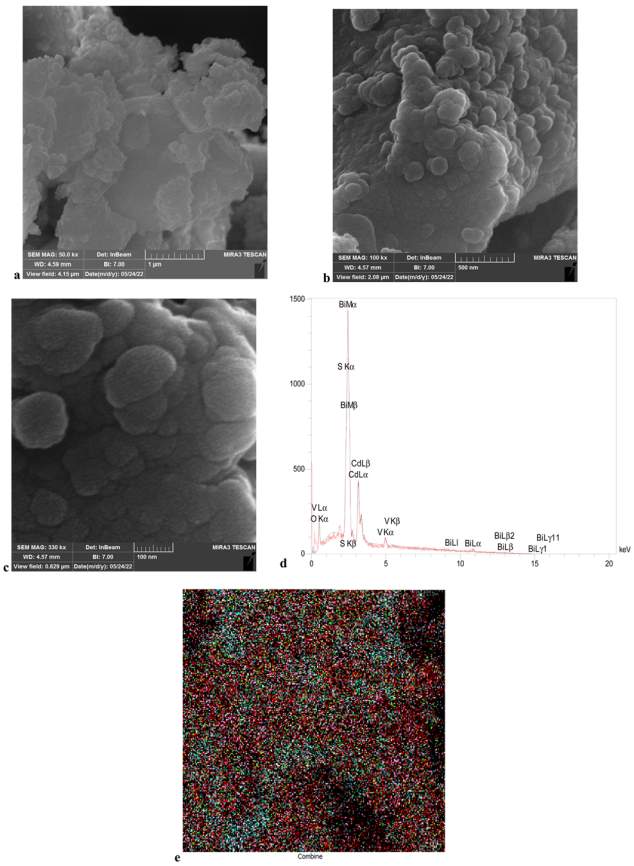

Fig. 2 SEM (A)–(C), EDX spectrum (D), and typical X-ray map (E) for the deposition prepared CdS/$BiVO_4$.[60,61]

3.2. Photodegradation experiments

3.2.1. Comparing the photodegradation activity of the coupled samples. The effect of the preparation method used to construct the binary BS catalysts in their photocatalytic ability toward EBT photodegradation was evaluated, and the corresponding UV-Vis spectra are shown in Fig. 3(A) and SDF4 (ESI†). As shown in the inset of Fig. 4(A), the lowest photocatalytic activity was observed for the BS catalyst prepared *via* simple mixing with no induced mechanical force. In this case, no significant connection between the CdS and $BiVO_4$ ingredients was created, and each component acted as an individual catalyst. In this case, even applying the ultrasonic force in hexane and water solvents could not make a suitable connection between the ingredients, and no significant enhancement was observed for these catalysts. Some absorption spectra were well discussed in our previous studies.[60,61] The effects of the change in the CdS : $BiVO_4$ molar ratio and the results showed that when this ratio changed from 1 : 1 to 1 : 4 in the

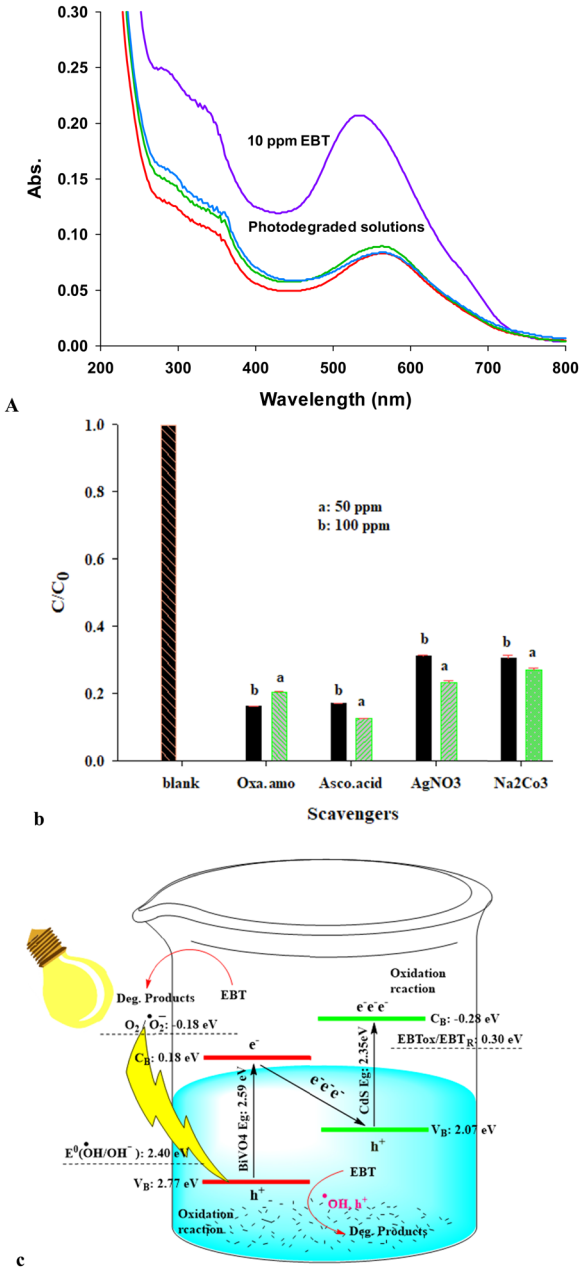

Fig. 3 (A) Typical UV-Vis spectra obtained in EBT photodegradation by the deposition prepared CdS/$BiVO_4$ photocatalyst, C_{EBT}: 10 ppm, catalyst dose: 0.3 g L^{-1}, irradiation time: 30 min, pH: 6.2 (inset: the photodegradation results obtained by the binary coupled photocatalysts prepared by various coupling methods, the results averaged based on triplicate measurements); (B) the effects of the scavenging agent in EBT photodegradation by Gr-BS catalyst (C_{EBT}: 15 ppm, catalyst dose: 0.9 g L^{-1}, irradiation time: 20 min, and pH: 7.3); (C) proposed Z-scheme charge carriers' transfer in the photo illuminated Gr-BS catalyst.

mechanically prepared catalyst, the highest photodegradation efficiency was achieved for the 1 : 1 ratio.[60] Thus, this ratio was applied to prepare the binary catalysts for the following strategies. In addition, the activity of the individual CdS and $BiVO_4$ NPs was compared with binary catalysts, and the results showed the boosted effects of the binary catalysts concerning the separate systems. For example, previously published papers have shown and discussed corresponding UV-Vis spectra for the EBT photodegraded solutions by the individual systems and mechanically prepared CdS–$BiVO_4$.[60]

In the second level, better photocatalytic activity was obtained by the binary BS catalyst fabricated *via* the grinding procedure. In this case, applying a mechanical force during the grinding of the mixture creates sufficient thermal energy to some extent to bind and connect CdS and $BiVO_4$ ingredients. This forms a boundary interface, inducing better charge carrier transfer between the photoexcited systems. In this case, applying ultrasonic (US) force in aqueous and organic solvents has no significant effect on the resulting BS system's activity. In these cases, applying US force may separate some connected CdS and $BiVO_4$ ingredients with weaker connections, negatively impacting the overall photocatalytic activity. In contrast, the applied US force may separate some aggregated BS species, resulting in a higher effective surface area as a positive impact on the overall activity of the photocatalyst. Thus, these positive and negative impacts are expected to have equal distributions in the overall activity of the WUS-Gr-BS and HUS-Gr-BS photocatalysts.

Finally, the BS catalyst prepared *via* deposition obtained the highest photocatalytic activity. Thus, this catalyst was selected for further investigation, and the effects of influencing variables in the overall photocatalytic activity were optimized *via* RSM as the most famous design experiment pathway. These results are illustrated in the following sections.

3.2.2. RSM test results. The RSM method was used for optimization to reach the best response level and determine the mutual effects of effective factors in pollutant degradation rate. For this purpose, Design Expert software (version 11) was used to design the test.[89] The experimental design method is used to overcome the two problems of lack of time and interaction of parameters, and the experimental design method is the best. In RSM, the experimental design is performed along with regression analysis. That is, the software designs the tests, and after entering the answers, it checks them statistically.[90]

Preliminary tests were conducted to obtain the pH range of the solution, pollutant concentration, the amount of catalyst used, and the duration of irradiation. Then, the test design was done with software using the response surface method to statistically design the tests, analyze the data, and optimize them.[91] The four main factors of pH, pollutant concentration, catalyst amount, and irradiation time were selected at five levels $-\alpha$ (minimum), -1, zero (central), $+1$, and $+\alpha$ (maximum) of the test according to Table 2.[92] The total number of tests with this method is equal to $2^k + 2k + c$, where k is the number of effective (main) factors in the efficiency of the process, which was chosen as 4 in this research. The design includes 24 tests in factorial points, 4 x^2 tests in central points, and the repetition rate of central points, which was considered equal to 6, and formed a total of 30 tests according to Table SDT4 (ESI†).[93]

3.2.2.1. Fit summary and ANOVA results. According to the stated relationships, the value of F obtained for the model is

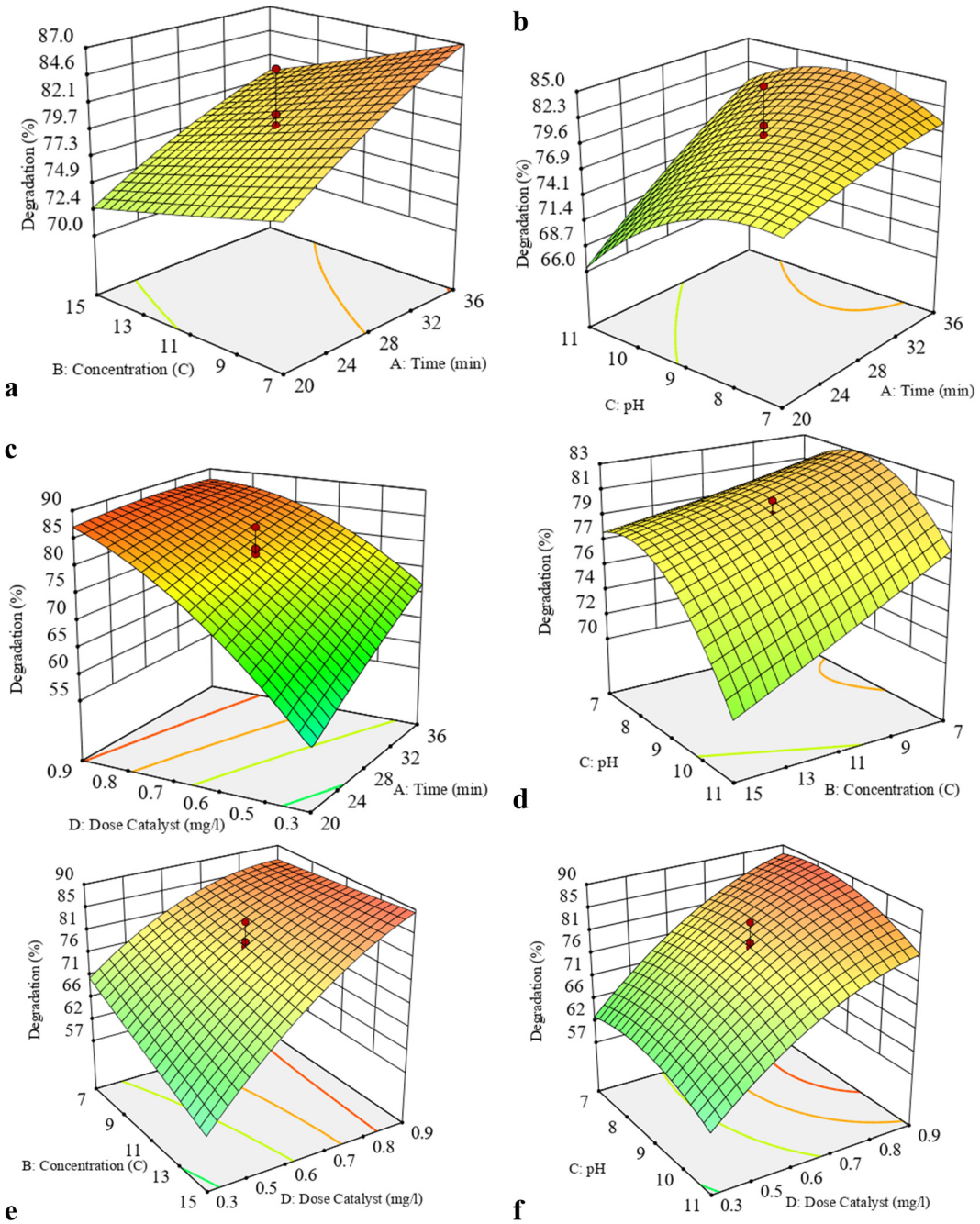

Fig. 4 3D response surface plots for showing simultaneous effects of the binary influencing factors in the EBT photodegradation by the D-BS photocatalyst.

65.38, much larger than the value ($F_{15,14,0.05}$) equal to 2.42, indicating that the suggested model is significant (Table 2). The answer obtained means that the percentage of degradation of Eriochrome black T is effective. Also, the F obtained for lack of fit is 0.39, which is less than ($F_{5,10,0.05}$), which is 4.47, indicating that the experiment's errors are due to random errors and the model is acceptable. The reported value for R^2 indicates the fit of the obtained experimental data with the proposed model. The closer this value is to one, the more acceptable it is. The value of R^2-Adj is the adjusted R^2 that includes the degree of freedom and should be close to the value of R^2. According to the obtained results, the R^2 value for the obtained answers was 0.9832, and the R^2 Adj value was 0.9460. The quantity of root mean square error and coefficient of variance or coefficient of change is a criterion for measuring the distribution of statistical data. An adequate accuracy parameter is obtained by dividing the difference between the most significant and minor predicted response by the average standard deviation of all predicted responses. This parameter measures the signal-to-noise ratio (S/N), and the model is accurate when

Table 2 Selected influencing variables, ANOVA table for the data obtained in the RSM study of EBT photodegradation by the proposed CdS/$BiVO_4$ catalyst

Code	Unite	−1 level	+1 level	−α	+α
A: C_{EBT}	mg L^{-1}	4	11	0.5	14.5
B: time	min	14	40	1	53
C: Cat. dose	g L^{-1}	0.35	0.9	0.075	1.175
D: pH	—	5	11	2	14

ANOVA table

Source	Sum Squares	df	Mean Square	*F* value	*p*-Value
Block	89.27	2	44.63		
Model	4365.55	14	311.82	110.61	>0.0001; sig.
A: C_{EBT}	408.38	1	408.38	144.85	>0.0001
B: time	260.04	1	260.04	92.24	>0.0001
C: dose	1855.04	1	1855.04	658.00	>0.0001
D: pH	532.04	1	532.04	188.72	>0.0001
AB	27.56	1	27.56	9.78	0.0080
AC	217.56	1	217.56	77.17	>0.0001
AD	39.06	1	39.06	13.86	0.0026
BC	10.56	1	10.56	3.75	0.0750
BD	95.06	1	95.06	33.72	>0.0001
CD	68.06	1	68.06	24.14	>0.0003
A^2	502.74	1	502.74	178.33	>0.0001
B^2	11.81	1	11.81	4.19	0.0614
C^2	75.24	1	75.24	26.69	0.0002
D^2	184.53	1	184.53	65.45	>0.0001
Residual	36.65	13	2.82		
Lack of fit	34.65	10	3.46	5.20	0.1008 not sig.
Pure error	2.00	3	0.67		
Cor total	4491.47	29			

Comparison between the experimental data and the suggested ones by the model

Variable	
Optimized values	pH 5, does: 0.9 g L^{-1}, C_{EBT}: 11 ppm, time: 40 min
Suggested model	Quadratic
Predicted response	96.07
95% CI low and high	93.63–98.52
Predicted std. dev.	2.02
Observed resp. (n = 3)	96 ± 0.267

Std. dev. 2.36, mean 63.60, C.V. 3.71%, PRESS 301.82, *R*-square 0.9861, adj *R*-square 0.9710, pred *R*-square 0.9417, adeq precision 28.103.

its value is greater than 4. This value was obtained for the results of 19.30.

The equation related to the degradation percentage of Eriochrome black T solution by catalyst D-BS based on the parameters mentioned in the ANOVA table (Table 2) is as follows.

$$D\% = +80.00\ b + 4.47\ A - 2.74\ B - 2.69\ C + 12.12\ D - 0.4437\ A \times B + 2.48\ A \times C - 4.04\ A \times D - 1.32\ C \times B + 3.96\ B * D - 0.6688\ C \times D - 0.6865\ A^2 + 0.0760\ B^2 - 3.32\ C^2 - 3.99\ D^2$$

Pareto analysis presents standardized effects in absolute values to examine which were positive or negative. Also, according to this diagram shown in SDF5 (ESI†), it is possible to see which parameters had the greatest impact on the degradation of the aqueous solution of Eriochrome black T. According to the following equation, the influence of each parameter on the response has been calculated, and the results are given in Fig. SDF5 (ESI†). According to the figure, it can be seen that (catalyst amount) had the greatest effect on the degradation of the blue solution of Eriochrome black T.

$$P_i = \left(\frac{b_i^2}{\sum b_i^2}\right) \times 100 \quad (i \neq 0)$$

3.2.2.2. 3D response surface plots. The graphs related to the interaction of two parameters that indicate the duration of time and the concentration of the pollutant are given in Fig. 4(A). The highest amount of degradation was achieved when the pollutant concentration was 11 ppm and the irradiation time was 27 minutes. According to the one-dimensional graphs, the resulting values show an increase in the pollutant concentration and a decrease in the duration of irradiation.

In Fig. 4(B), the 3D graphs of the response show the interactions of initial pH and the irradiation time in EBT photodegradation. The highest percentage of degradation of EBT is at medium pH and less than 8 and irradiation times of 20 minutes. As can be seen in the figure, it is obvious that the

percentage of degradation increased with the increase of irradiation time, which indicates that in the initial stages of degradation, intermediates that have high ratio stability may be produced. These intermediates may be degraded for longer times.

The simultaneous effect of the amount of catalyst and the time is shown in Fig. 4(C). The highest amount of degradation was achieved when the amount of catalyst used was around 0.9 g L^{-1} and the irradiation time was around 20 minutes. Both parameters in the interaction with the degradation of EBT showed an increasing value compared to the one-dimensional state.

In Fig. 4(D), the 3D graph shows the interaction of the initial pH of the EBT concentration with its photodegradation extent. It is observed that, with decrease in pH and EBT concentration, the degradation extent has increased. The interaction between the two parameters caused the degradation percentage to be significant at pH values lower than 8 and concentrations higher than 6 mg L^{-1}. Considering that the pHpzc of the combined $CdS/BiVO_4$ photocatalyst is equal to 7.6 (shown in SDF5, ESI†), at this pH value, the aqueous solution of Eriochrome black T exists in a neutral form and the surface of the catalyst is positive, so there is an attraction between positive charges and non-bonded electrons in Eriochrome black T. Electrostatics have occurred. The desired combined catalyst has degraded Eriochrome black T at a lower pH. Also, at concentrations less than 7 mg L^{-1}, radicals are not produced enough for destruction. At higher concentrations, the accumulation of pollutant molecules prevents the passage of radiation and reduces the active surface for destruction.

In Fig. 4(E), the 3D graph shows the effects of interactions of the catalyst dose and the EBT concentration in the overall EBT photodegradation efficiency. The highest EBT degradation extent is due to the constructive interaction of the EBT concentration and the amount of photocatalyst observed in the concentration range higher than 7 mg L^{-1} of EBT and the amount of photocatalyst between 0.3 and 0.9 g L^{-1}. The amount of destruction increases up to the optimal value along with the increase in pollutant concentration, and it can be said that due to the increase of hydroxyl radicals produced with high amounts of photocatalyst, this high volume of $^{\bullet}OH$ enters into the reaction by high pollutant concentrations. As it is clear in the graphs, with the increase in the number of photocatalysts, the efficiency of the photodegradation process increases. It reaches the maximum value at the optimal value of 0.9 g L^{-1} and then decreases. Increasing the amount of photocatalyst increases the number of photocatalyst particles, which increases the number of active sites for producing electron–hole pairs. Also, the photocatalyst adsorbs more pollutant molecules, and the degradation percentage of EBT increases. On the other hand, by increasing the amount of photocatalyst from the optimal value, the turbidity of the solution increases, which makes the photons emitted from the lamp unable to reach the lower parts of the solution, and only the photocatalysts in the upper parts of the solution are located where the light will hit them and produce electron holes. As a result, the amount of $^{\bullet}OH$ is reduced, and the amount of destruction is reduced. Also, in amounts higher than the optimal amount of photocatalyst, these particles are interconnected due to particle–particle interaction, which causes the scattering of photons. As a result, fewer electrons and holes are produced, which has reduced the destruction in large amounts of photocatalysts.

Fig. 4(F) shows the change in the EBT degradation percentage due to simultaneous interactions of the initial pH and the amount of photocatalyst. The highest EBT degradation is due to the constructive interaction of pH, the amount of photocatalyst at pH less than 8, and the amount of photocatalyst 0.35 to 0.9 mg L^{-1}. According to the available results, increasing the amount of photocatalyst up to 0.9 g L^{-1} increases the photodegradation efficiency because it increases the number of active sites for hole–electron production. Also, the photocatalyst adsorbs more pollutant molecules and the EBT degradation percentage increases.

The effect of pH on the surface charge and the formation of ionic forms is due to the substituents' deprotonation and protonation in the EBT molecule's structure. At very low pH, the surface charge of the photocatalyst is positive. According to the pK_a of EBT (6.2), the cationic form is dominant at these pHs. The repulsion between positive charges causes the rejection of EBT molecules from the surface of the photocatalyst, and the degradation rate decreases. This effect becomes more serious at low amounts of photocatalysts because the available sites are also reduced. At pH 7 to 5 (pHpzc equal to 7.6), this problem still exists, but increasing the amount of photocatalyst provides more sites, and the rate of degradation increases.

3.2.3. Effects of scavenging agents. The effects of some potential scavenging agents on the efficiency of the D-BS catalyst were studied and the results are compared in Fig. 3(B). In general, some inorganic species scavenge the e/h pairs and decrease their recombination rate, resulting in boosted photocatalytic activity. In contrast, some scavengers scavenge the produced reactive radicals and the e/h pairs, reducing the overall photocatalytic activity.[16]

By scavenging the photo-excited electrons, silver nitrate produces nitrate anion radicals that are less active than the powerful hydroxyl radicals. Furthermore, it retards the e/h recombination *via* this scavenging process. In this study, ascorbic acid (AA) acts as a superoxide radical scavenger, oxalate as the hole scavenger, and carbonate as the hydroxyl radical scavenger. The results confirmed that in the presence of all scavenging agents, the overall photodegradation efficiency decreased, especially in the presence of oxalate and AA agents. Thus, the holes and superoxide radicals played a vital role in the EBT photodegradation by the proposed D-BS catalyst, followed by photoinduced electrons and hydroxyl radicals. Based on the results observed in Fig. 3(B), if the relative role of all reactive species is high, the following trend can be suggested for their relative roles in EBT photodegradation by the proposed catalyst.

$$\text{Superoxide} \approx \text{holes} > \text{electrons} \approx \text{hydroxyl radicals}$$

Accordingly, a Z-scheme mechanism was proposed to elucidate the charge carrier's transfer in the photo-illuminated D-BS

catalyst in EBT photodegradation, as shown in Fig. 3(C). In this mechanism, the photo-excited electrons in the CB-$BiVO_4$ with more negative potential position of 0.18 V can be transferred to the VB-CdS position (E: 2.07 V) and then photo-excited to its CB position. Overall charge carriers' transfer in this system accumulates the photoexcited electrons in the CB-CdS position with a potential of −0.28 V, which are more potent than the electrons in the CB-$BiVO_4$ position with a potential position of 0.12 V. Following this pathway, the photoinduced holes leave in the VB-$BiVO_4$ with a possible position of 2.77 V which are more potent than the holes in the VB-CdS (E: 2.07 V). It is worth mentioning that in a type II-heterojunction mechanism pathway, the photoexcited electrons accumulate in the CB-$BiVO_4$ position, and the holes in the CB-CdS position are both less active than the corresponding positions occupied in the direct Z-Scheme pathway.

The preferential role of the superoxide radicals is because of the accumulation of the photoinduced electrons in the CdS-CB position (E: −0.28 V), which can reduce the dissolved oxygen to superoxide radicals. In addition, these accumulated electrons also have enough potential to degrade EBT molecules *via* a reduction pathway. On the other hand, if a type(II) heterojunction mechanism is proposed, it accumulates photoinduced electrons in CB-$BiVO_4$, which potentially cannot produce superoxide radicals according to the potential positions, and superoxide radical can be created only in the direct Z-scheme mechanism charge transfer not in a type II-heterogeneous pathway.

In the proposed direct Z-scheme mechanism, the accumulated holes in the VB-$BiVO_4$ are stronger agents than those collected in the CdS-VB (*via* a type(II) heterojunction mechanism) to oxidize water molecules or hydroxyl anions to the powerful hydroxyl radicals. Thus, enough hydroxyl radicals can be produced in the direct Z-scheme mechanism. These accumulated electrons in VB-$BiVO_4$ are also strong enough to degrade EBT molecules. Detailed illustrations for various charge carriers transfer, including direct Z-scheme, S-scheme *etc.*, have been illustrated or reviewed well in the literature.[39,94–98]

3.2.4. Kinetics and COD experiments. To have some kinetic information about the EBT photodegradation process, photodegradation reactions were done at various illumination times ranging from 0 to 30 min in 5 min steps under the conditions of pH: 7.3, catalyst dose: 0.9 g L^{-1}, and C_{EBT}: 9.5 ppm. The following EBT degradation percentages were obtained: 0, 20, 30, 65, 80, 84, and 90%. The results (as C/C_0) were then substituted into the Hinshelwood model,[99] and the linear equation plot of $y = -0.0614x + 0.1713$, $r^2 = 0.9543$ was obtained, confirming the Hinshelwood model is suitable for investigating the process kinetically. The slope of the curve shows the pseudo-first-order rate constant, $k = -0.0614$ min^{-1}.

In the next step, the above EBT photodegraded solutions were applied in the COD (chemical oxygen demand) experiments. The results showed that the initial COD of 32 mgO_2 per L (at time 0) decreased 28.8, 24, 16, 14.4, 8, and 8 after 5 to 30 min photodegradation. Based on the COD results, the EBT degradation percentages were calculated as 0, 10, 25, 50, 55, 75, and 75% respectively. The COD data (as [CPD]/[COD]o instead of C/C_0) were substituted into the Hinshelwood model and the linear equation plot $y = -0.0517x + 0.1098$, $r^2 = 0.9534$ was obtained. The k value of -0.0517 min^{-1} is close to the k value of -0.0614 min^{-1} obtained by UV-Vis data in the photodegraded solutions. This means that EBT molecules and their degradation intermediate have been relatively mineralized to water, carbon dioxide, *etc.*, during photodegradation. This conclusion is based on the fact that if large EBT degradation intermediates remained in the photodegraded solution, COD amounts would be expected to be high.

3.2.5. Reusability results. The reusability experiment was also done under the optimal photodegradation conditions (pH: 7.3, catalyst dose: 0.9 g L^{-1}, C_{EBT}: 9.5 ppm, illumination time: 20 min) because this is a crucial issue from economic and environmental points of view. In this step, the photocatalyst was recovered at the end of each run, and after washing, it was dried at 80 °C for 20 min and used in the next run. The EBT degradation extents of 88.1 (± 3.2)%, 86.3 (± 2.5)%, 83 (± 3.4)%, and 79.2 (± 2.9)% were obtained for the first to the fourth reusing runs based on triplicate measurements. The results are reasonable for a typical photodegradation catalyst, confirming the high stability of the catalyst under the applied conditions.

3.2.6. Comparison with other studies. So far, some photocatalysts have been used to detect EBT photodegradation. Among them, we can mention Pt and Fe doped TiO_2,[100] TiO_2-biochar composite,[101] ZnO,[102] NiO–ZnO,[103] SnO_2,[104] CeO_2,[105] electro-Fenton,[106] Fenton,[107] *etc.* Despite the advantages of the suggested catalysts, some have a wide band gap energy located in the UV region of light. In addition, TiO_2, especially in a nanoscale, can hardly be separated from the suspension at the end of the process. The Fenton process critically has a pH-dependence efficiency and needs severe acidic conditions to prevent Fe-hydroxide salts. In these hard acidic pHs, the catalyst may dissolve. If higher pHs are applied, in addition to decreased activity due to Fe-hydroxide precipitation, a secondary removal process should be applied to separate this sludge. Here, the catalyst has a short band gap which can be excited under solar and visible light. In addition, the preparation method is easy and CdS can be easily deposited on the surface of $BiVO_4$ in a simple precipitation method.

4. Conclusions

Crystallite sizes of 25.3 and 45 nm were obtained using the Scherrer and W–H models, confirming the effect of the induced strain in the preparation of binary catalysts. SEM images showed the particle size in the 56–97 nm range. The difference observed between XRD data and SEM images is that SEM gives particle sizes, and particles consist of some crystallites. The lowest photocatalytic activity was observed for the BS catalyst prepared *via* simple mixing with no induced mechanical force. In this case, no significant connection between the CdS and $BiVO_4$ ingredients was created, and each component acted as

an individual catalyst. Even applying the ultrasonic force in both hexane and water solvents could not create a suitable connection between the ingredients, and no significant enhancement was observed for these catalysts. In the second level, better photocatalytic activity was obtained by the binary BS catalyst fabricated *via* the grinding procedure, which applied a mechanical force to create sufficient thermal energy to bind and connect CdS and $BiVO_4$ ingredients to some extent, forming a boundary interface between them, inducing better charge carriers transfer between the photoexcited systems. In this case, applying ultrasonic (US) force in aqueous and organic solvents has no significant effect on the resulting BS system's activity. In these cases, applying US force may separate some connected CdS and $BiVO_4$ ingredients with weaker connections, negatively impacting the overall photocatalytic activity. In contrast, the applied US force may separate some aggregated BS species, resulting in a higher effective surface area as a positive impact on the overall activity of the photocatalyst. Thus, these positive and negative impacts are expected to have equal distributions in the overall activity of the WUS-Gr-BS and HUS-Gr-BS photocatalysts. Finally, the BS catalyst prepared *via* deposition obtained the highest photocatalytic activity. The following trend can be suggested for the relative roles of reactive species in EBT photodegradation by the proposed catalyst.

$$\text{Superoxide} \approx \text{holes} > \text{electrons} \approx \text{hydroxyl radicals}$$

Accordingly, a Z-scheme mechanism was proposed to elucidate the charge carrier's transfer in the photo-illuminated D-BS catalyst in EBT photodegradation. Overall, charge carriers' transfer in this system accumulates the photoexcited electrons in the CB-CdS position with a potential of −0.28 V, which are more potent than the electrons in the CB-$BiVO_4$ position with a potential position of 0.12 V. The photoinduced holes left in the VB-$BiVO_4$ have a potential position of 2.77 V, which is more potent than the holes in the VB-CdS (*E*: 2.07 V).

Data availability

All required data are summarized in the ESI.†

Conflicts of interest

There are no conflicts to declare.

Acknowledgements

The authors thank Mohammad Alizadeh and Mohammad Hossein Kazemzadeh for performing instrumental analysis of the samples, as experts in laboratory analysis in Shahreza Branch, Islamic Azad University, Isfahan, Iran. The authors also thank the university president for supporting of this work.

References

1 R. Al-Tohamy, S. S. Ali, F. Li, K. M. Okasha, Y. A. G. Mahmoud, T. Elsamahy, H. Jiao, Y. Fu and J. Sun, A critical review on the treatment of dye-containing wastewater: Ecotoxicological and health concerns of textile dyes and possible remediation approaches for environmental safety, *Ecotoxicol. Environ. Saf.*, 2022, **231**, 113160.
2 V. Chandanshive, S. Kadam, N. Rane, B.-H. Jeon, J. Jadhav and S. Govindwar, In situ textile wastewater treatment in high rate transpiration system furrows planted with aquatic macrophytes and floating phytobeds, *Chemosphere*, 2020, **252**, 126513.
3 A. Singh, A. K. Singh, J. Liu and A. Kumar, Syntheses, design strategies, and photocatalytic charge dynamics of metal–organic frameworks (MOFs): a catalyzed photodegradation approach towards organic dyes, *Catal. Sci. Technol.*, 2021, **11**, 3946–3989.
4 J. Dai, G. Xie, X. Huo, J. Li, S. Deng and Y. Su, Implantable and Biodegradable Smart Textiles for Continuous Limb and Gastrointestinal Motility Monitoring, *Small*, 2025, 2407773.
5 J. Wang, C. Rao, L. Lu, S. Zhang, M. Muddassir and J. Liu, Efficient photocatalytic degradation of methyl violet using two new 3D MOFs directed by different carboxylate spacers, *CrystEngComm*, 2021, **23**, 741–747.
6 M. Liu, C. Shan, H. Chang, Z. Zhang, R. Huang, D. W. Lee, W. Qi, Z. He and R. Su, Nano-engineered natural sponge as a recyclable and deformable reactor for ultrafast conversion of pollutants from water, *Chem. Eng. Sci.*, 2022, **247**, 117049.
7 S. Thangaraj, P. O. Bankole and S. K. Sadasivam, Microbial degradation of azo dyes by textile effluent adapted, Enterobacter hormaechei under microaerophilic condition, *Microbiol. Res.*, 2021, **250**, 126805.
8 J. Zhao, Z. Dang, M. Muddassir, S. Raza, A. Zhong, X. Wang and J. Jin, A New Cd(II)-Based Coordination Polymer for Efficient Photocatalytic Removal of Organic Dyes, *Molecules*, 2023, **28**(19), 6848.
9 K. Singha, P. Pandit, S. Maity and S. R. Sharma, Chapter 11 – Harmful environmental effects for textile chemical dyeing practice, in *Green Chemistry for Sustainable Textiles*, ed. N. Ibrahim and C. M. Hussain, Woodhead Publishing, 2021, pp. 153–164.
10 H. Arshad, M. Imran and M. Ashraf, Toxic effects of Red-S3B dye on soil microbial activities, wheat yield, and their alleviation by pressmud application, *Ecotoxicol. Environ. Saf.*, 2020, **204**, 111030.
11 A. M. Elgarahy, K. Z. Elwakeel, S. H. Mohammad and G. A. Elshoubaky, A critical review of biosorption of dyes, heavy metals and metalloids from wastewater as an efficient and green process, *Clean. Eng. Technol.*, 2021, **4**, 100209.
12 P. Manickam and D. Vijay, 2 – Chemical hazards in textiles, in *Chemical Management in Textiles and Fashion*, ed. S. S. Muthu, Woodhead Publishing, 2021, pp. 19–52.

13 J. Feng, C. E. Cerniglia and H. Chen, Toxicological significance of azo dye metabolism by human intestinal microbiota, *Front. Biosci., Elite Ed.*, 2012, **4E**, 568–586.
14 K. Pompapathi, K. S. Anantharaju, P. Karuppasamy, M. Subramaniam, B. Uma, S. Boppanahalli Siddegowda, A. Paul Chowdhury and H. C. A. Murthy, Visible-Light-Driven Mentha spicata L.-Mediated Ag-Doped $Bi_2Zr_2O_7$ Nanocomposite for Enhanced Degradation of Organic Pollutants, Electrochemical Sensing, and Antibacterial Applications, *ACS Environ. Au*, 2024, **4**, 106–125.
15 R. Kishor, D. Purchase, G. D. Saratale, R. G. Saratale, L. F. R. Ferreira, M. Bilal, R. Chandra and R. N. Bharagava, Ecotoxicological and health concerns of persistent coloring pollutants of textile industry wastewater and treatment approaches for environmental safety, *J. Environ. Chem. Eng.*, 2021, **9**, 105012.
16 P. Karuppasamy, S. Senthilkumar, O. Ganeshbabu, S. Pitchaimuthu, M. Sennappan and V. Rajapandian, Sonochemical Synthesis and Characterization of Visible Light Driven CuO@g-C_3N_4 Nano-Photocatalyst for Eriochrome Black T Dye Degradation in Industrial Dye Effluent, *Russ. J. Inorg. Chem.*, 2022, **67**, 2153–2165.
17 A. M. El-Khawaga, M. A. Elsayed, M. Gobara, A. A. Suliman, A. H. Hashem, A. A. Zaher, M. Mohsen and S. S. Salem, Green synthesized ZnO nanoparticles by Saccharomyces cerevisiae and their antibacterial activity and photocatalytic degradation, *Biomass Convers. Biorefin.*, 2025, **15**, 2673–2684.
18 F. Ullah, Z. Ul Haq Khan, S. Sabahat, M. Aftab, J. Sun, N. Samad Shah, A. Rahim, M. M. S. Abdullah and M. Imran, Synergistic degradation of toxic azo dyes using Mn-CuO@Biochar: An efficient adsorptive and photocatalytic approach for wastewater treatment, *Chem. Eng. Sci.*, 2025, **302**, 120844.
19 E. Rápó, K. Posta, A. Csavdári, B. É. Vincze, G. Mara, G. Kovács, I. Haddidi and S. Tonk, Performance Comparison of Eichhornia crassipes and Salvinia natans on Azo-Dye (Eriochrome Black T) Phytoremediation, *Crystals*, 2020, **10**(7), 565.
20 Z. Liu, J. Liu, Y. Tian, Y. Hu and Q. Zou, A novel catalyst $Zn_{0.5}Cu_{0.5}Fe_2O_4/C_3N_4$ photocatalytic synergistic activation of persulfate for efficient degradation of Eriochrome black T, *Ceram. Int.*, 2025, **51**, 7411–7419.
21 J. Huang, G. Xie, X. Xu, Z. Geng and Y. Su, Degradable Multilayer Fabric Sensor with Wide Detection Range and High Linearity, *ACS Appl. Mater. Interfaces*, 2024, **16**, 58838–58847.
22 J. Huang, Y. Cai, G. Xie, X. Xu, Z. Geng, Y. Jiang and Y. Su, Hierarchical carbon nanotube-decorated polyacrylonitrile smart textiles for wearable biomonitoring, *Wearable Electron.*, 2024, **1**, 180–188.
23 Y. Su, Y. Liu, W. Li, X. Xiao, C. Chen, H. Lu, Z. Yuan, H. Tai, Y. Jiang, J. Zou, G. Xie and J. Chen, Sensing–transducing coupled piezoelectric textiles for self-powered humidity detection and wearable biomonitoring, *Mater. Horiz.*, 2023, **10**, 842–851.
24 T. Shindhal, P. Rakholiya, S. Varjani, A. Pandey, H. H. Ngo, W. Guo, H. Y. Ng and M. J. Taherzadeh, A critical review on advances in the practices and perspectives for the treatment of dye industry wastewater, *Bioengineered*, 2021, **12**, 70–87.
25 P. Karuppasamy, N. Ramzan Nilofar Nisha, A. Pugazhendhi, S. Kandasamy and S. Pitchaimuthu, An investigation of transition metal doped TiO_2 photocatalysts for the enhanced photocatalytic decoloration of methylene blue dye under visible light irradiation, *J. Environ. Chem. Eng.*, 2021, **9**, 105254.
26 S. Samsami, M. Mohamadizaniani, M.-H. Sarrafzadeh, E. R. Rene and M. Firoozbahr, Recent advances in the treatment of dye-containing wastewater from textile industries: Overview and perspectives, *Process Saf. Environ. Prot.*, 2020, **143**, 138–163.
27 H. Li, Y. Ding, K. Luo, Q. Zhang, H. Yuan, S. Xu and M. Xu, Controllable surface carrier type of metal oxide nanocrystals for multifunctional photocatalysis, *iScience*, 2025, **28**(2), 111750.
28 W. Chen, R.-Q. Yan, G.-H. Chen, M.-Y. Chen, G.-B. Huang and X.-H. Liu, Hydrothermal route to synthesize helical CdS@$ZnIn_2S_4$ core–shell heterostructures with enhanced photocatalytic hydrogeneration activity, *Ceram. Int.*, 2019, **45**, 1803–1811.
29 R.-q Yan, G.-h Liu, Q.-f Wang, W. Liu and C.-l Song, Fast Photodegradation of Malachite Green using Nano-ZnO on Ceramic MgAl Carbonate Layered Double Hydroxides Support, *Chin. J. Chem. Phys.*, 2016, **29**, 241–244.
30 M. Liu, Y. Ye, J. Ye, T. Gao, D. Wang, G. Chen and Z. Song, Recent Advances of Magnetite (Fe_3O_4)-Based Magnetic Materials in Catalytic Applications, *Magnetochemistry*, 2023, **9**(4), 110.
31 R. Xiang, C. Zhou, Y. Liu, T. Qin, D. Li, X. Dong, M. Muddassir and A. Zhong, A new type Co(II)-based photocatalyst for the nitrofurantoin antibiotic degradation, *J. Mol. Struct.*, 2024, **1312**, 138501.
32 D. Ye, L. Liu, Q. Peng, J. Qiu, H. Gong, A. Zhong and S. Liu, Effect of Controlling Thiophene Rings on D–A Polymer Photocatalysts Accessed *via* Direct Arylation for Hydrogen Production, *Molecules*, 2023, **28**(11), 4507.
33 X. Dong, Y. Li, D. Li, D. Liao, T. Qin, O. Prakash, A. Kumar and J. Liu, A new 3D 8-connected Cd(II) MOF as a potent photocatalyst for oxytetracycline antibiotic degradation, *CrystEngComm*, 2022, **24**, 6933–6943.
34 P. Dhull, A. Sudhaik, V. Sharma, P. Raizada, V. Hasija, N. Gupta, T. Ahamad, V.-H. Nguyen, A. Kim, M. Shokouhimehr, S. Y. Kim, Q. V. Le and P. Singh, An overview on $InVO_4$-based photocatalysts: Electronic properties, synthesis, enhancement strategies, and photocatalytic applications, *Mol. Catal.*, 2023, **539**, 113013.
35 Z. Pan, S. Wang, R. Yan, C. Song, Y. Jin, G. Huang and J. Huang, Enhanced photocatalytic properties of Mn doped CdS catalysts by decomposition of complex precursors, *Opt. Mater.*, 2020, **109**, 110324.
36 M. Liu, Y. Wan, C. Zhu, G. Chen and X. Li, FeNi bimetallic modified pg-C_3N_4-*x* and its photoelectrocatalytic hydrogen

production coupling anodic oxidation, *Sep. Purif. Technol.*, 2025, **357**, 130142.

37 C. Rao, L. Zhou, Y. Pan, C. Lu, X. Qin, H. Sakiyama, M. Muddassir and J. Liu, The extra-large calixarene-based MOFs-derived hierarchical composites for photocatalysis of dye: Facile syntheses and contribution of carbon species, *J. Alloys Compd.*, 2022, **897**, 163178.

38 Y. Wu, X. He, X. Wang, J. Xv, M. Muddassir, I. A. Ansari and A. Zhong, Synergistic efficacy unleashed: Co/Ni-based catalysts as a versatile powerhouse for photocatalytic degradation of ornidazole, *Inorg. Chim. Acta*, 2024, **568**, 122115.

39 H. Yang, Z.-C. Zhao, Y.-P. Yang, Z. Zhang, W. Chen, R.-Q. Yan, Y. Jin and J. Zhang, Defective WO_3 nanoplates controllably decorated with MIL-101(Fe) nanoparticles to efficiently remove tetracycline hydrochloride by S-scheme mechanism, *Sep. Purif. Technol.*, 2022, **300**, 121846.

40 K. Sharma, A. Kumar, T. Ahamad, Q. V. Le, P. Raizada, A. Singh, L. H. Nguyen, S. Thakur, V.-H. Nguyen and P. Singh, Sulphur vacancy defects engineered metal sulfides for amended photo(electro)catalytic water splitting: A review, *J. Mater. Sci. Technol.*, 2023, **152**, 50–64.

41 B. Liu, A. Libanori, Y. Zhou, X. Xiao, G. Xie, X. Zhao, Y. Su, S. Wang, Z. Yuan, Z. Duan, J. Liang, Y. Jiang, H. Tai and J. Chen, Simultaneous Biomechanical and Biochemical Monitoring for Self-Powered Breath Analysis, *ACS Appl. Mater. Interfaces*, 2022, **14**, 7301–7310.

42 J. Liu, L. Qiu, M.-J. Chang, B. Yuan, M. Sun, S.-M. Fan, W.-N. Cui, Q. Hui, F.-R. Ni and M.-Y. Li, Fabrication of novel fibrous $BiVO_4$/CdS heterostructures by electrospinning method for efficient visible light photodegradation, *Mater. Chem. Phys.*, 2020, **247**, 122858.

43 M. Lv, S. Wang and H. Shi, Carbon quantum dots/BiVO4 S−scheme piezo−photocatalysts improved carrier separation for efficient antibiotic removal, *J. Mater. Sci. Technol.*, 2024, **201**, 21–31.

44 Z. Kása, E. E. Almási, K. Hernádi, T. Gyulavári, L. Baia, G. Veréb, Z. László and Z. Pap, New insights into the photoactivity of shape-tailored $BiVO_4$ semiconductors *via* photocatalytic degradation reactions and classical reduction processes, *Molecules*, 2020, **25**(20), 4842.

45 H. L. Tan, R. Amal and Y. H. Ng, Alternative strategies in improving the photocatalytic and photoelectrochemical activities of visible light-driven $BiVO_4$: A review, *J. Mater. Chem. A*, 2017, **5**, 16498–16521.

46 Y. Park, K. J. Mc Donald and K. S. Choi, Progress in bismuth vanadate photoanodes for use in solar water oxidation, *Chem. Soc. Rev.*, 2013, **42**, 2321–2337.

47 A. Hekmat, S. Ghasemi and M. Vossoughi, Unveiling the synergistic effect of ionic liquid and metal-organic framework on the efficiency of $BiVO_4$: $BiVO_4$-MIL-100(Fe) as a visible light-induced photocatalyst for Basic Red 46 degradation, *J. Environ. Chem. Eng.*, 2023, **11**, 110658.

48 Y. Xue, Z. Chen, Z. Wu, F. Tian and B. Yu, Hierarchical construction of a new *Z*-scheme Bi/$BiVO_4$–CdS heterojunction for enhanced visible-light photocatalytic degradation of tetracycline hydrochloride, *Sep. Purif. Technol.*, 2021, **275**, 119152.

49 T. D. Nguyen and S.-S. Hong, Facile solvothermal synthesis of monoclinic-tetragonal heterostructured $BiVO_4$ for photodegradation of rhodamine B, *Catal. Commun.*, 2020, **136**, 105920.

50 L. Zou, H. Wang, C. Wu, L. Li, G. Yuan and X. Wang, Construction of all-solid-state *Z*-scheme 2D $BiVO_4$/Ag/CdS composites with robust photoactivity and stability, *Appl. Surf. Sci.*, 2019, **498**, 143900.

51 Z.-H. Wei, Y.-F. Wang, Y.-Y. Li, L. Zhang, H.-C. Yao and Z.-J. Li, Enhanced photocatalytic CO_2 reduction activity of *Z*-scheme CdS/$BiVO_4$ nanocomposite with thinner $BiVO_4$ nanosheets, *J. CO2 Util.*, 2018, **28**, 15–25.

52 Y. Li, X. Li, X.-T. Wang, L.-J. Jian, N. I. M. Abdallah, X.-F. Dong and C.-W. Wang, Pn Heterostructured design of decahedral NiS/$BiVO_4$ with efficient charge separation for enhanced photodegradation of organic dyes, *Colloids Surf., A*, 2021, **608**, 125565.

53 M. Song, Y. Wu, C. Xu, X. Wang and Y. Su, Synergistic effects of multi-active sites in silver modified Bi^{0}-$BiVO_4$ toward efficient reduction of aromatic nitrobenzene, *J. Hazard. Mater.*, 2019, **368**, 530–540.

54 A. Yousefi and A. Nezamzadeh-Ejhieh, Preparation and characterization of SnO_2–$BiVO_4$–CuO catalyst and kinetics of phenazopyridine photodegradation, *Iran. J. Catal.*, 2024, **11**(3), 247–259.

55 I. Ahmad, S. Ben Ahmed, M. Shabir, M. Imran, A. M. Hassan and N. S. Alatawi, Review on CdS-derived photocatalysts for solar photocatalytic applications – Advances and challenges, *J. Ind. Eng. Chem.*, 2024, **130**, 105–124.

56 A. Qian, X. Han, C. Situ, M. Fan, Q. Liu, X. Pu, J. Liu, J. Zhang, J. Zhan and B. Hu, Photocatalytic hydrogen production using novel noble-metal-free NiMo/CdS photocatalysts with hollow nanospheres structure, *Mol. Catal.*, 2024, **555**, 113878.

57 L. Wang, J. Liu, W. Song, H. Wang, Y. Li, J. Liu, Z. Zhao, J. Tan, Z. Duan and J. Deng, Experimental and DFT insights of $BiVO_4$ as an effective photocatalytic catalyst for N_2O decomposition, *Chem. Eng. J.*, 2019, **366**, 504–513.

58 O. A. Sánchez, J. L. Rodríguez, J. M. Barrera-Andrade, R. Borja-Urby and M. A. Valenzuela, High performance of Ag/$BiVO_4$ photocatalyst for 2,4-Dichlorophenoxyacetic acid degradation under visible light, *Appl. Catal., A*, 2020, **600**, 117625.

59 M. Sun, Q. Zeng, X. Zhao, Y. Shao, P. Ji, C. Wang, T. Yan and B. Du, Fabrication of novel g-C3N4 nanocrystals decorated Ag_3PO_4 hybrids: Enhanced charge separation and excellent visible-light driven photocatalytic activity, *J. Hazard. Mater.*, 2017, **339**, 9–21.

60 P. Hemmatpour, A. Nezamzadeh-Ejhieh and A. Ershadi, A brief study on the Eriochrome Black T photodegradation kinetic by CdS/$BiVO_4$ coupled catalyst, *Mater. Res. Bull.*, 2022, **151**, 111830.

61 P. Hemmatpour and A. Nezamzadeh-Ejhieh, A *Z*-scheme CdS/$BiVO_4$ photocatalysis towards Eriochrome black T: An

experimental design and mechanism study, *Chemosphere*, 2022, **307**, 135925.

62 N. Qutub, B. M. Pirzada, K. Umar and S. Sabir, Synthesis of CdS nanoparticles using different sulfide ion precursors: formation mechanism and photocatalytic degradation of Acid Blue-29, *J. Environ. Chem. Eng.*, 2016, **4**, 808–817.

63 S. Selvarajan, A. Suganthi, M. Rajarajan and K. Arunprasath, Highly efficient BiVO4/WO3 nanocomposite towards superior photocatalytic performance, *Powder Technol.*, 2017, **307**, 203–212.

64 Z. Wu, Y. Xue, X. He, Y. Li, X. Yang, Z. Wu and G. Cravotto, Surfactants-assisted preparation of BiVO4 with novel morphologies *via* microwave method and CdS decoration for enhanced photocatalytic properties, *J. Hazard. Mater.*, 2020, **387**, 122019.

65 T. Tamiji and A. Nezamzadeh-Ejhieh, A comprehensive study on the kinetic aspects and experimental design for the voltammetric response of a Sn(IV)-clinoptilolite carbon paste electrode towards Hg(II), *J. Electroanal. Chem.*, 2018, **829**, 95–105.

66 B. Gao, Y. Pan, Q. Chang, Z. Xi and H. Yang, Hierarchically *Z*-scheme photocatalyst of {010}BiVO4/Ag/CdS with enhanced performance in synergistic adsorption-photodegradation of fluoroquinolones in water, *Chem. Eng. J.*, 2022, **435**, 134834.

67 R. Ranjith, N. Karmegam, M. Alsawalha, X. Hu and K. Jothimani, Construction of g-C_3N_4/CdS/$BiVO_4$ ternary nanocomposite with enhanced visible-light-driven photocatalytic activity toward methylene blue dye degradation in the aqueous phase, *J. Environ. Manage.*, 2023, **330**, 117132.

68 J. Liu, L. Qiu, M.-J. Chang, B. Yuan, M. Sun, S.-M. Fan, W.-N. Cui, Q. Hui, F.-R. Ni, M.-Y. Li, Y.-Q. Li and Z.-M. Luo, Fabrication of novel fibrous $BiVO_4$/CdS heterostructures by electrospinning method for efficient visible light photodegradation, *Mater. Chem. Phys.*, 2020, **247**, 122858.

69 Y. Lin, D. Pan and H. Luo, Hollow direct *Z*-Scheme CdS/$BiVO_4$ composite with boosted photocatalytic performance for RhB degradation and hydrogen production, *Mater. Sci. Semicond. Process.*, 2021, **121**, 105453.

70 F. Q. Zhou, J. C. Fan, Q. J. Xu and Y. L. Min, BiVO4 nanowires decorated with CdS nanoparticles as *Z*-scheme photocatalyst with enhanced H_2 generation, *Appl. Catal., B*, 2017, **201**, 77–83.

71 G. Xu, M. Du, T. Li, Y. Guan and C. Guo, Facile synthesis of magnetically retrievable Fe_3O_4/BiVO4/CdS heterojunction composite for enhanced photocatalytic degradation of tetracycline under visible light, *Sep. Purif. Technol.*, 2021, **275**, 119157.

72 T. Seyedi-Chokanlou, S. Aghabeygi, N. Molahasani and F. Abrinaei, Applying Taguchi method to optimize the synthesis conditions of ZrO_2/TiO_2/ZnO nanocomposite for high-performance photodegradation of Congo red, *Iran. J. Catal.*, 2024, **11**(1), 49–58.

73 E. Yalçın and M. Dükkancı, Ternary CuS@Ag/$BiVO_4$ composite for enhanced photo-catalytic and sono-photocatalytic performance under visible light, *J. Solid State Chem.*, 2022, **313**, 123319.

74 R. J. Kalbasi, A. R. Massah and A. Shafiei, Synthesis and characterization of BEA-SO_3H as an efficient and chemoselective acid catalyst, *J. Mol. Catal. A: Chem.*, 2011, **335**, 51–59.

75 N. Clament Sagaya Selvam, Y. G. Kim, D. J. Kim, W.-H. Hong, W. Kim, S. H. Park and W.-K. Jo, Reduced graphene oxide-mediated *Z*-scheme $BiVO_4$/CdS nanocomposites for boosted photocatalytic decomposition of harmful organic pollutants, *Sci. Total Environ.*, 2018, **635**, 741–749.

76 J. Huang, Y. Ma, Q. Chen, J. Zhu, H. Jiang, H. Li, L. Yi, H. Li and M. Hong, Effect of water-oil ratio on the photocatalytic performance of visible light-active $BiVO_4$ nanoparticles prepared by inverse microemulsion–calcination method, *Chemosphere*, 2022, **299**, 134454.

77 C. Ma, Z. Xie, W. C. Seo, S. T. Ud Din, J. Lee, Y. Kim, H. Jung and W. Yang, Carbon dot-coupled $BiVO_4$/reduced graphene hydrogel for significant enhancement of photocatalytic activity: Antibiotic degradation and CO_2 reduction, *Appl. Surf. Sci.*, 2021, **565**, 150564.

78 M. Arunkumar and A. Samson Nesaraj, Photocatalytic degradation of malachite green dye using NiAl2O4 and Co doped $NiAl_2O_4$ nanophotocatalysts prepared by simple one pot wet chemical synthetic route, *Iran. J. Catal.*, 2024, **10**(3), 235–245.

79 B. Manikandan, K. R. Murali and R. John, Optical, Morphological and Microstructural Investigation of TiO_2 nanoparticles for Photocatalytic application, *Iran. J. Catal.*, 2024, **11**(1), 1–11.

80 N. Omrani and A. Nezamzadeh-Ejhieh, A quadripartite Cu_2O–CdS–BiVO4–WO_3 visible-light driven photocatalyst contained three cascade *Z*-scheme systems: Focus on conditions' optimization, scavenging agents and the mechanism pathway towards sulfasalazine, *Iran. J. Catal.*, 2025, DOI: 10.57647/j.ijc.2025.1502.15.

81 S. K. Suram, P. F. Newhouse and J. M. Gregoire, High Throughput Light Absorber Discovery, Part 1: An Algorithm for Automated Tauc Analysis, *ACS Comb. Sci.*, 2016, **18**, 673–681.

82 P. Norouzzadeh, K. Mabhouti, M. Golzan and R. Naderali, Investigation of structural, morphological and optical characteristics of Mn substituted Al-doped ZnO NPs: a Urbach energy and Kramers-Kronig study, *Optik*, 2020, **204**, 164227.

83 P. Makuła, M. Pacia and W. Macyk, How To Correctly Determine the Band Gap Energy of Modified Semiconductor Photocatalysts Based on UV-Vis Spectra, *J. Phys. Chem. Lett.*, 2018, **9**, 6814–6817.

84 J. Tauc, in *Chap. 5 of Optical Properties of Solids*, ed. F. Abeles, North-Holland Publishing Company, Amsterdam, 1972.

85 J. B. Coulter and D. P. Birnie III, Assessing Tauc Plot Slope Quantification: ZnO Thin Films as a Model System, *Phys. Status Solidi B*, 2018, **255**, 1700393.

86 R. Köferstein, L. Jäger and S. G. Ebbinghaus, Magnetic and optical investigations on $LaFeO_3$ powders with different

particle sizes and corresponding ceramics, *Solid State Ionics*, 2013, **249–250**, 1–5.

87 R. Köferstein and S. G. Ebbinghaus, Investigations of $BaFe_{0.5}Nb_{0.5}O_3$ nano powders prepared by a low temperature aqueous synthesis and resulting ceramics, *J. Eur. Ceram. Soc.*, 2017, **37**, 1509–1516.

88 K.-i Katsumata, R. Motoyoshi, N. Matsushita and K. Okada, Preparation of graphitic carbon nitride (g-C_3N_4)/WO_3 composites and enhanced visible-light-driven photodegradation of acetaldehyde gas, *J. Hazard. Mater.*, 2013, **260**, 475–482.

89 P. Eskandari, E. Amarloo, H. Zangeneh, M. Rezakazemi and T. M. Aminabhavi, Photocatalytic degradation of metronidazole and oxytetracycline by novel l-Arginine (C, N codoped)-TiO_2/g-C_3N_4: RSM optimization, photodegradation mechanism, biodegradability evaluation, *Chemosphere*, 2023, **337**, 139282.

90 T. Musabeygi, N. Goudarzi, M. Mirzaee and M. Arab-Chamjangali, Design of a ternary magnetic composite based on a covalent organic framework and Ag nanoparticles for simultaneous photodegradation of organic pollutants under LED light irradiation: Application of BBD-RSM modeling and resolution of spectral overlap of analytes, *J. Alloys Compd.*, 2023, **964**, 171249.

91 M. Hasanpour, S. Motahari, D. Jing and M. Hatami, Statistical analysis and optimization of photodegradation efficiency of methyl orange from aqueous solution using cellulose/zinc oxide hybrid aerogel by response surface methodology (RSM), *Arabian J. Chem.*, 2021, **14**, 103401.

92 S. Deylami, M. H. Sabzevari, M. Ghaedi, M. H. A. Azqhandi and F. Marahel, Efficient photodegradation of disulfine blue dye and Tetracycline over Robust and Green g-CN/Ag_3VO_4/PAN nanofibers: Experimental design, RSM, RBF-NN and ANFIS modeling, *Process Saf. Environ. Prot.*, 2023, **169**, 71–81.

93 H. Mirhosseini, A. Mostafavi and T. Shamspur, Highly efficient LaFeO3/Bi_2WO_6 *Z*-scheme nanocomposite for photodegradation of tetracycline under visible light irradiation: Statistical modeling and optimization of process by CCD-RSM, *Mater. Sci. Semicond. Process.*, 2023, **160**, 107413.

94 Z.-C. Zhao, K. Wang, L. Chang, R.-Q. Yan, J. Zhang, M. Zhang, L. Wang, W. Chen and G.-B. Huang, Construction of S-scheme MIL-101(Fe)/Bi_2MoO_6 heterostructures for enhanced catalytic activities towards tetracycline hydrochloride photodegradation and nitrogen photofixation, *Sol. Energy*, 2023, **264**, 112042.

95 V. Dutta, S. Sonu, P. Raizada, V. K. Thakur, T. Ahamad, S. Thakur, P. Kumar Verma, H. H. P. Quang, V.-H. Nguyen and P. Singh, Prism-like integrated Bi_2WO_6 with Ag-$CuBi_2O_4$ on carbon nanotubes (CNTs) as an efficient and robust S-scheme interfacial charge transfer photocatalyst for the removal of organic pollutants from wastewater, *Environ. Sci. Pollut. Res.*, 2023, **30**, 124530.

96 Y. Kumar, A. Sudhaik, K. Sharma, Sonu, P. Raizada, A. Aslam Parwaz Khan, V.-H. Nguyen, T. Ahamad, P. Singh and A. M. Asiri, Construction of magnetically separable novel arrow down dual S-scheme $ZnIn_2S_4$/BiOCl/$FeVO_4$ heterojunction for improved photocatalytic activity, *J. Photochem. Photobiol., A*, 2023, **435**, 114326.

97 M. Malhotra, K. Poonia, P. Singh, A. A. P. Khan, P. Thakur, Q. Van Le, E. T. Helmy, T. Ahamad, V.-H. Nguyen, S. Thakur and P. Raizada, An overview of improving photocatalytic activity of MnO_2 *via* the *Z*-scheme approach for environmental and energy applications, *J. Taiwan Inst. Chem. Eng.*, 2024, **158**, 104945.

98 K. Sharma, V. Hasija, M. Malhotra, P. K. Verma, A. A. Parwaz Khan, S. Thakur, Q. Van Le, H. H. Phan Quang, V.-H. Nguyen, P. Singh and P. Raizada, A review of CdS-based S-scheme for photocatalytic water splitting: Synthetic strategy and identification techniques, *Int. J. Hydrogen Energy*, 2024, **52**, 804–818.

99 A. S. Nesaraj and A. Samson Nesaraj, Reflux condensation synthesis and characterization of Co_3O_4 nanoparticles for photocatalytic applications, *Iran. J. Catal.*, 2024, **4**(4), 219–226.

100 B. Pal, R. Kaur and I. S. Grover, Superior adsorption and photodegradation of eriochrome black-T dye by Fe^{3+} and Pt^{4+} impregnated TiO_2 nanostructures of different shapes, *J. Ind. Eng. Chem.*, 2016, **33**, 178–184.

101 M. Abdu, S. Tibebu, S. Babaee, A. Worku, T. A. M. Msagati and J. F. Nure, Optimization of photocatalytic degradation of Eriochrome Black T from aqueous solution using TiO_2-biochar composite, *Results Eng.*, 2025, **25**, 104036.

102 R. H. Waghchaure, V. A. Adole and B. S. Jagdale, Photocatalytic degradation of methylene blue, rhodamine B, methyl orange and Eriochrome black T dyes by modified ZnO nanocatalysts: A concise review, *Inorg. Chem. Commun.*, 2022, **143**, 109764.

103 M. Karimi-Shamsabadi, M. Behpour, A. K. Babaheidari and Z. Saberi, Efficiently enhancing photocatalytic activity of NiO–ZnO doped onto nanozeoliteX by synergistic effects of p–n heterojunction, supporting and zeolite nanoparticles in photo-degradation of Eriochrome Black T and Methyl Orange, *J. Photochem. Photobiol., A*, 2017, **346**, 133–143.

104 M. Najjar, H. A. Hosseini, A. Masoudi, Z. Sabouri, A. Mostafapour, M. Khatami and M. Darroudi, Green chemical approach for the synthesis of SnO_2 nanoparticles and its application in photocatalytic degradation of Eriochrome Black T dye, *Optik*, 2021, **242**, 167152.

105 S. Mishra, S. Soren, A. K. Debnath, D. K. Aswal, N. Das and P. Parhi, Rapid microwave – Hydrothermal synthesis of CeO_2 nanoparticles for simultaneous adsorption/photodegradation of organic dyes under visible light, *Optik*, 2018, **169**, 125–136.

106 H. Belbel, R. Delimi, Z. Benredjem, K. Barbari and L. Rabah, Degradation of Eriochrome Black T by heterogeneous electro-Fenton: a comparison study, *Desalin. Water Treat.*, 2023, **314**, 219–230.

107 E. Hadinejad, S. Hashemian and S. A. Yasini, Comparison of catalytic effect of Fe-MOF and Fe-ZIF for Fenton degradation of Eriochrome black T, *Desalin. Water Treat.*, 2017, **90**, 180–188.